Pergamon

Cement and Concrete Research 29 (1999) 1027–1037

CEMENT AND CONCRETE RESEARCH

Modeling the pullout of wire-drawn steel fibers☆

Gilles Chanvillard*

ENTPE Département Génie Civil et Batiment, URA CNRS 1652, Vaulx en Velin, France

Received 15 December 1998; accepted 24 March 1999

Abstract

Previously, the emphasis when modeling the behavior of the pullout of an individual fiber anchored in a cement-based matrix was on bond-stress-slip relationships. In case of fibers with nonstraight geometries, such modeling approaches present obvious limitations. In this paper, a micromechanical model has been developed taking into account the different phenomena observed during pullout of a nonstraight fiber, including the mechanisms of steel deformation. Model's parameters are fitted, based on experiments carried out on specially made fibers. Finally, applications of the model to the geometries of commercialized fibers are presented. The good performances that were obtained in comparison with pullout tests confirms the validity of the chosen approach. It opens the door to a modeling of fiber behavior based on a knowledge of characteristics of the fibers themselves and to an optimization of fiber geometries.

Keywords: Steel fiber; Cement-based composite; Fiber geometry; Modeling; Friction; Cohesion; Steel hardening; Pullout test

The incorporation of steel fibers in a cement-based matrix enables a considerable amount of energy to be dissipated during structural cracking. Because of the wide variety of commercialized fibers available, numerous results have been obtained without always being able to correlate them according either to their dosages in fibers, to the fiber distribution in the matrix, or in particular to the fiber geometry.

Wire-drawn fibers, which represent the majority of fibers currently being used, have a similar behavior when they are pulled out of a matrix sample. Indeed, these fibers are progressively debonded, slipping until they emerge—a process that causes them to straighten out [1,2].

Paradoxically, modeling such behavior is often limited to considerations of cohesion of the fiber-matrix interface [3–9]. The limitations imposed by generalizing in this way to analyze the behavior of fiber-reinforced concrete become obvious when one takes parameters such as fiber orientation into account.

We propose to independently model each of the phenomenon observed during the experiments in order to more accurately describe the actual behavior of a fiber. Several physical parameters are therefore necessary and sufficient for our model to be generalized for all the wire-drawn fibers. In the end, a validation on the most common geometries qualitatively and quantitatively confirms the performances of the model.

1. Model development

1.1. Mechanical balance

To build the model, the general case of a small fiber element having a given curvature will be examined [2,10–13]. The static equilibrium of external forces on this element can be written in the following manner [Eq. (1)]:

$$\text{along the x-axis:} \quad dP \cdot \cos(d\theta/2) = dT \tag{1}$$

$$\text{along the z-axis:} \quad P \cdot \sin(d\theta/2) + (P + dP) \cdot \sin(d\theta/2) = dN \tag{2}$$

Thus, because of the curvature, a radial component dN appears. In fact, this is more of a normal stress to the fiber-matrix interface. We can easily see that this stress is not uniformly spread out over the perimeter of the fiber and probably corresponds to a compression on the concave part of the fiber and a tension on the convex part. Our reasoning here is in terms of global forces, corresponding to stress integration on the fiber element's surface. In the same manner, the tangential component dT corresponds to the tangential stress that develops along the fiber element.

☆ This paper was originally submitted to *Advanced Cement Based Materials.* The paper was received at the Editorial Office of *Cement and Concrete Research* on 15 December 1998 and accepted in final form on 24 March 1999.

* Corresponding author. Tel.: +334-7204-7080; fax: +334-7204-7156.
E-mail address: gilles.chanvillard@entpe.fr (G. Chanvillard)

0008-8846/99/$ – see front matter
PII: S0008-8846(99)00081-2

Taking Eq. (2), given that for small angles $\sin(d\theta/2) = d\theta/2$, $\cos(d\theta/2) = 1$ and ignoring higher order terms, we therefore have Eq. (3) and Eq. (4):

along the x-axis: $$dP = dT \tag{3}$$

along the z-axis: $$dN = P \cdot d\theta \tag{4}$$

1.2. Energy balance sheet during slipping

Experimentally, there is no doubt that steel is deformed during nonstraight fiber slipping. A particular case of this observation is the fiber inclined with respect to the crack plane [1,2,14–18]. Consequently, the purely static approach of the fiber balance does not permit an assessment of the energy dissipated during the slipping. The equilibrium of this fiber element curve must therefore be studied from an energy point of view. Here, mass forces such as gravity are disregarded.

The balance of the mechanical energies, applied to the slipping fiber element, enables us to state that the work done by the external forces (W_{ext}) is equal to the deformation energy dissipated (W_{def}) [Eq. (5)]:

$$W_{ext} = W_{def} \tag{5}$$

The work of external forces is generally written as Eq. (6):

$$W_{ext} = \int_s p_i \cdot u_i \cdot dS \tag{6}$$

and corresponds to an integral over the element's external surface of the product of elementary stress p_i (pressure exerted on the exterior surface) and the kinematics displacement field of the element, *ui* (the *i* index represents a coordinate in space).

In the same manner, the deformation energy can be written as Eq. (7):

$$W_{def} = \int_v \sigma_{ij} \cdot \varepsilon_{ij} \cdot dV \tag{7}$$

and corresponds to an integral over the element's volume V of the product of the stress tensor, σ_{ij} and stain tensor, ϵ_{ij}.

To assess each of these two terms, a "u_i" licit kinematics displacement field of the fiber element that slips must be stated. Later this will allow us to calculate the strain tensor. Physically, during slipping a fiber element undergoes (Fig. 1): slipping, as a rigid body, of amplitude $d\delta$. In fact, this displacement corresponds to the integral of elastic strain all along the fiber, to which is added the overall slipping of the fiber's anchored end bending, which produces a variation in the curvature dC in such a way that the fiber slips in the print of its initial geometry. This displacement field resulting from bending can be written expressed in the mobile coordinate system (s,x,y) in such a way as to directly eliminate the fiber element rigid body displacement [Eq. (8)]:

$$u \begin{cases} u_s = z \cdot s \cdot dC \\ u_z = 0 \\ u_y = 0 \end{cases} \tag{8}$$

where s is the curvilinear coordinate, z is the radial coordinate such that the fiber is bent in the plane (s,z), and y is the coordinate that is perpendicular to the plane (s,z)

All the external forces are represented in Fig. 2. It is obvious that along with the displacement field examined here, only the stress components according to the curvilinear axis are operational, that is P, $P + dP$ and dT (here, we are examining the global forces).

Thus, the relationship of Eq. (6), with Eq. (8), and taking into account the rigid body displacement, becomes Eq. (9):

$$\begin{aligned} W_{ext} = & -\frac{P}{S}\int_s \left(d\delta + z \cdot \left(s - \frac{ds}{2}\right) \cdot dC\right) \cdot dS \\ & + \frac{(P + dP)}{S}\int_s \left(d\delta + z \cdot \left(s + \frac{ds}{2}\right) \cdot dC\right) \cdot dS \\ & - \frac{dT}{S'}\int_{s'} (d\delta + z \cdot s \cdot dC) \cdot dS' \end{aligned} \tag{9}$$

where S is the surface of the section of the fiber [plane (z,y)] and S' is the fiber friction surface on the matrix (Fig. 3).

Consequently, by disregarding the terms of higher order [see Eq. (10)], there remains:

$$W_{ext} = -P \cdot d\delta + (P + dP) \cdot d\delta - dT \cdot d\delta \tag{10}$$

which simplifies to Eq. (11):

$$W_{ext} = dP \cdot d\delta - dT \cdot d\delta \tag{11}$$

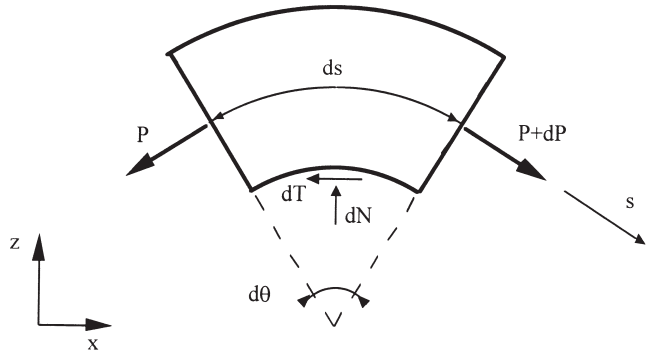

Fig. 1. Illustration of small element displacement.

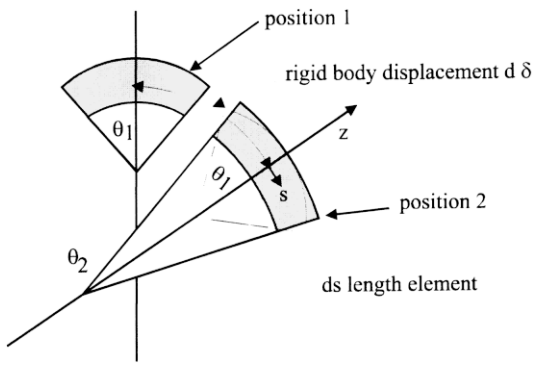

Fig. 2. Equilibrium of a small fiber element.

Using the adopted licit displacement field [Eq. (8)], the strain tensor can also be calculated. Here, we will consider that the strains, even if they are plastic (fiber break is not considered), may be expressed in a small strains formulation [Eq (12)], that is, that:

$$\varepsilon_{ij} = \frac{1}{2}(\partial_j u_i + \partial_i u_j) \tag{12}$$

We then obtain the strain tensor, with the relationships to Eqs. (8) and (12), as Eq. (13):

$$[\varepsilon_{ij}] = \begin{bmatrix} z \cdot dC & \frac{1}{2}s \cdot dC & 0 \\ \frac{1}{2}s \cdot dC & 0 & 0 \\ 0 & 0 & 0 \end{bmatrix} \tag{13}$$

To assess the deformation energy, we must have a good estimate of the stress state in the fiber element. This results, on one hand, from the axial stress that produces a traction assumed to be uniform over all the section and, on the other hand, of a change in curvature that produces "bending" (traction and compression). Finally, shear components exist, essentially caused by friction of the fiber-matrix contact (considering a small element uniformly supported by the matrix, shear reaction is neglected). We can assume that the latter remain insignificant in the energy balance sheet.

Superposing these two stress states leads to a nonsymmetrical axial stress distribution along the fiber's section (i.e., that the neutral axis of the stress no longer coincides with the geometrical axis). It is even more difficult to know the real stress state, because of these plastification phenomena.

Thus, the stress tensor σ_{ij} takes the form shown in Eq. (14):

$$[\sigma_{ij}] = \begin{bmatrix} \sigma & 0 & 0 \\ 0 & 0 & 0 \\ 0 & 0 & 0 \end{bmatrix} \tag{14}$$

where σ is the stress governed by the ϵ strain state.

We can now assess the deformation energy W_{def}, with the relationships demonstrated in Eqs. (7), (13), and (14), as shown in Eq. (15):

$$W_{def} = \int_v z \cdot dC \cdot \sigma \cdot dV \tag{15}$$

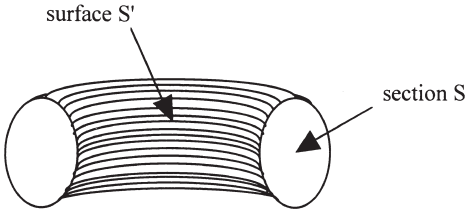

Fig. 3. Definition of integration surfaces on a fiber element.

or even, by considering that the curvature variation is constant for a sufficiently short fiber element [see Eq. (16)]:

$$W_{def} = dC \cdot ds \int_s z \cdot \sigma \cdot dS \tag{16}$$

where ds is the curvilinear element length and dS is the section element.

In Eq. (16), again we find two terms. First, the term ($dC \cdot ds$), which represents an angular variation $d^2\theta$ and, on the other hand, a set that corresponds to the bending moment M produced by stress distribution. In addition, this state of stress must also equate to the normal pullout load [see Eq. (17)], meaning:

$$P(s) = \int_s \sigma \cdot dS \tag{17}$$

Considering that for a given curvature, a unique stress state exists that balances the axial load P, the moment M may be obtained with interaction diagrams established on the basis of a constitutive equation.

We must then adopt a constitutive equation for steel that would introduce the phenomenon of plasticity. The most general case consists of adopting an elastic plastic constitutive equation with hardening (EPE). In fact, the idea of hardening (the outflow stress varies according to the extent of strain) is complex to introduce in an analytical calculation. Moreover, the perfectly plastic elastic constitutive equation (PPE) is usually preferable to the EPE equation (Fig. 4). Such behavior follows Hooke's Law up to a proportional limit and then begins to plastify itself, under constant stress.

In our case, each fiber element has its own history (i.e., that the initial stress state is unknown to us, even before experimentation). Furthermore, what we would like to evaluate here is the dissipated energy. Consequently, it is difficult to take into account the energy that is absorbed and then restituted (domain of elastic behavior), as well as the loading and unloading phenomena, in the residual stress states.

Based on the PPE behavior law, we have been able to assess the curvature-normal load-bending moment interaction diagrams (Fig. 5). On this figure, N is the normal load and Np is the axial capacity of the fiber.

For simplicity, a moment-curvature-normal stress bilinear

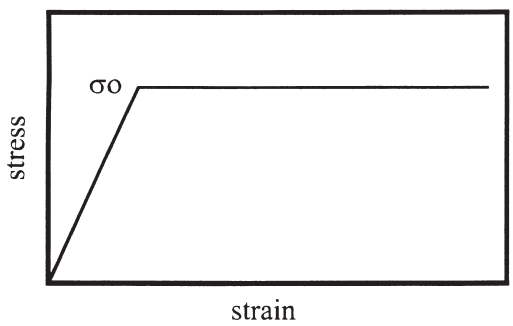

Fig. 4. PPE constitutive equation.

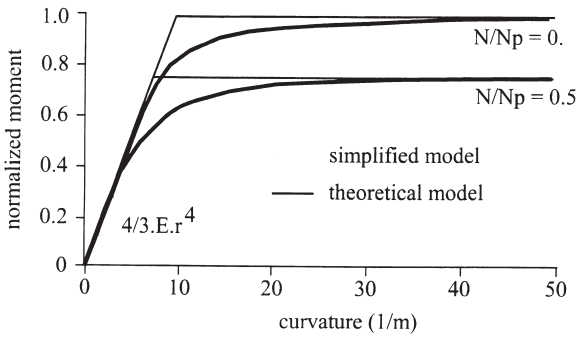

Fig. 5. Curvature-normal load-bending moment interaction diagram.

model was chosen for later developments, which is represented by the lines in Fig. 5. Furthermore, the moment-normal load interaction diagram corresponding to large curvatures, illustrated on Fig. 6, was fitted using a third degree polynomial, shown in Eq. (18):

$$M = Mp(1 - 0.0539(N/Np) - 0.7156(N/Np)^2 - 0.2304(N/Np)^3) \quad (18)$$

where M is the bending moment and Mp the plastic moment of the fiber section.

Finally, a physical modification was carried out on the preceding model to take into account the progressive mobilization of plastification energy as the fiber slips. Indeed, even if we consider that the fiber slips according to the print of its initial geometry, it would be realistic to consider that the change in curvature will only be effective beyond a certain minor displacement due to a local adaptation of the matrix to the fiber. Consequently, a moment-relative slip relationship enables this effect to be taken into account (Fig. 7).

The balance of the mechanical energy can then be written, with relationships to Eqs. (5), (11), and (16), as Eq. (19):

$$dP \cdot d\delta - dT \cdot d\delta = M \cdot dC \cdot ds \quad (19)$$

This equation supplies us with a relationship between the external stresses applied on the fiber and the energy that is dissipated through steel deformation as it slips. This is the basis for our theoretical modeling of fiber-slipping behavior.

1.3. Modeling the behavior of the fiber-matrix contact

We have seen that the balance of momentum of a fiber element as it slips would generate a dN radial component and a dT friction component (Fig. 2). Therefore, these two forces can be linked by a friction law. However, this approach remains complex and we will not enter into specific physical details here.

The simplest manner to formulate this law is known as Coulomb's law of friction and consists of linking the shear stress, τ, to the normal stress, σ, of a facet using a friction coefficient f and a cohesion Co [see Eq. (20)]:

$$\tau = Co + \sigma \cdot f \quad (20)$$

Thus, we will adopt Coulomb's law in global forces, as in Eq. (21):

$$dT = f \cdot dN + \tau o \cdot p \cdot ds \quad (21)$$

where p is the perimeter of the fiber and τo is the bond stress between the fiber and the matrix.

With such a formulation, notions of friction-cohesion coefficients will be generalized, since we do not actually take into account the distribution of normal and tangential stresses.

1.4. Final formulation of the model

By combining the Eqs. (4), (19), and (21), we have Eq. (22):

$$dP \cdot d\delta = (\tau o \cdot p \cdot ds + f \cdot P \cdot C \cdot ds) \cdot d\delta + M \cdot dC \cdot ds \quad (22)$$

that can also be written as Eq. (23):

$$dP = (\tau o \cdot p + f \cdot P \cdot C + M \cdot C')ds \quad (23)$$

where C' is the first derivative of the curvature C against the curvilinear abscissa.

A differential equation of the first order in P is obtained. Consequently, we can then conclude that the mechanical anchorage phenomena, due to the fiber's geometry and friction, are intimately linked.

The interaction between these two effects signifies that one cannot consider that the fiber's behavior results in an

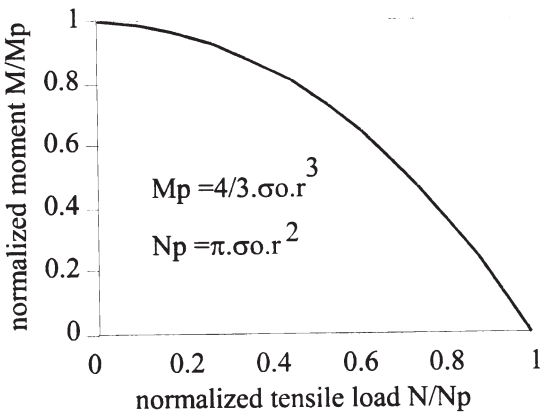

Fig. 6. Moment-normal load interaction diagram for large curvature.

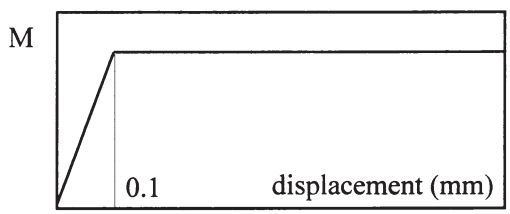

Fig. 7. Moment-relative displacement model.

anchorage component and a friction component, on an overall scale of the fiber. It is necessary to work at the scale of a fiber element and then integrate the micromechanical model along the fiber.

1.5. Modeling of the cohesion

Physically, the idea of cohesion results from strong links that develop during hydration of the cement at the fiber-matrix contact. Modeling this phenomenon was carried out in a classical fashion in reference to the shear lag theory [4,5,7,8,19–22]. It consists of adopting a relationship defining cohesion stress according to the relative slip of the fiber in relation to the matrix (Fig. 8).

This relationship has two stages. First, a nonlinear behavior up to τ_{max} maximum cohesion stress. The fiber is not really debonded during this stage and the relative slip is assessed by examining the difference between the set of average strains in the fiber and in the matrix. Then, the fiber debonds and cohesion decreases to a residual stress that originates in the microstructural bridging activated as the fiber slips [8,22]. The residual stress was taken, in an arbitrary fashion, as being equal to half τ_{max} ($\tau_{lim} = 50\%$).

It is obvious that this residual stress is not constant for all the possible configurations [6]. In the case of nonstraight fibers, we will see that this nuance plays a secondary role in overall behavior. According to previous works [3,9], an average relative displacement δo have been taken as being equal to 0.01 mm.

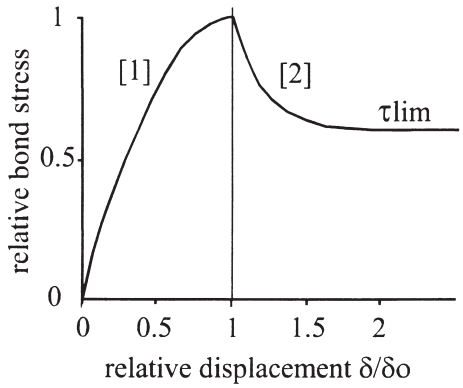

$$[1]: \frac{\tau_o}{\tau\,\max} = 1 - \left(1 - \frac{\delta}{\delta o}\right)^2$$

$$[2]: \frac{\tau_o}{\tau\,\max} = (1 - \tau\,\lim)\exp\left(\alpha \frac{\left(1 - \frac{\delta}{\delta 0}\right)}{(1 - \tau\,\lim)}\right) + \tau\,\lim$$

$$\delta o = 0.01\text{mm}$$

Fig. 8. Cohesion-slip relationship.

1.6. Modeling of the friction

The friction coefficient incorporated in the model enables an assessment to be made of the average shear stress, activated in the fiber-matrix interface, according to the intensity of normal average stress. By analogy with the preceding cohesion stress, a friction coefficient-slip relationship of the fiber is proposed (Fig. 9).

Here again, two stages can be distinguished. The first one, corresponding to an activation of the friction coefficient, describes the bridging mechanism that develops in the fiber-matrix interface after debonding and according to irregularities in the crack pattern. The second stage, corresponding to a softening in the mechanism on the friction coefficient, can be explained by polishing aspects in the interface after a break in the maximum bridging ($f = f_{max}$). The friction coefficient decreases to a limit value defined in fraction of f_{max} ($f = f_{lim} \cdot f_{max}$).

We will see that this polishing concept at the fiber-matrix interface plays a dominant role in the behavior of nonstraight fiber pullout.

1.7. Integrating the model

The micromechanical model presents itself in the form of a differential equation [Eq. (23)]. We must integrate this equation along the anchored part of the fiber to obtain the theoretical pullout load-displacement curve.

The integration path consists in divided the fiber in small element of length *ds*. At each step of integration, the parameters of the model are calculated in function of the previous step, relative displacement. Then *dP* is obtained and *P* is increased with *dP*. Further, the relative displacement is cor-

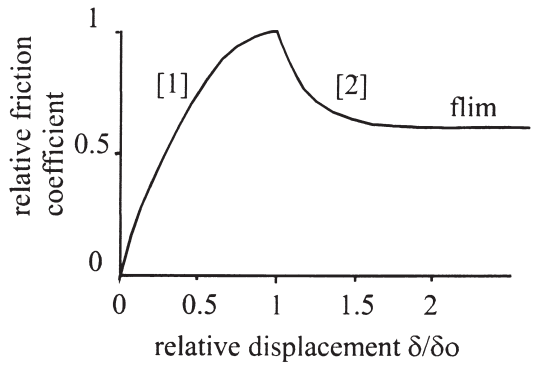

$$[1]: \frac{f}{f\,\max} = 1 - \left(1 - \frac{\delta}{\delta o}\right)^2$$

$$[2]: \frac{f}{f\,\max} = (1 - f\,\lim)\exp\left(\alpha \frac{\left(1 - \frac{\delta}{\delta 0}\right)}{(1 - f\,\lim)}\right) + f\,\lim$$

Fig. 9. Friction coefficient-slip relationship.

rected with the integration of the average fiber axial strain. The next step of integration follows.

Practically, this integration is a two-step process. First, we know that fiber debonding is progressive. It would be sufficient to consider the successive debonding abscissa by starting with the crack area and continuing toward the anchored end of the fiber. By establishing P equals few newtons, to allow the model to start with nonzero parameters values as a limit value at the level of the debonded abscissa, the model is integrated from this abscissa to the crack. The relative displacement of the fiber head can then be obtained by integration of the axial strain of the fiber.

When the fiber is completely debonded, it would be sufficient to consider the successive positions of the fiber during pullout, which gives the relative displacement of the anchor end. By always establishing a very small value for P as the limit value to this anchored end, integration of the model is carried out along an length that gets smaller and smaller as pullout progresses. In this case, the relative slip of the fiber corresponds to the total displacement of the fiber's extremity and of the integration of the fiber axial strain. This latter term very quickly becomes negligible.

2. Applying the model on elementary fiber geometries

2.1. The case of a straight fiber

Within the framework of an initial experimental program, straight fibers of various diameters were tested and anchored in matrices of varying natures:

fiber diameters: 0.6 and 1.0 mm

matrices: slurry (w/c 0.6); slurry (w/c 0.4); mortar (w/c 0.5, sand 5 mm)

Fig. 10 illustrates the typical behavior during pullout of a fiber 40-mm long and 1 mm in diameter anchored in mortar. The model was able to be fitted in order to obtain the values of the τ_{max} cohesion stress (Table 1).

Applying the model generated the dotted curve in Fig. 10, which is in accordance with the experimental results. It should be mentioned that in the case of straight fiber, the present model is coherent with classical published models [8,9]. Following this initial experimental program, it appeared that cohesion stress values are independent of fiber

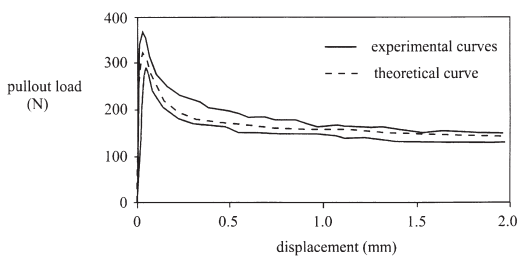

Fig. 10. Pullout load-displacement curve in case of a straight fiber (length 40 mm, diameter 1 mm, mortar).

Table 1
Cohesion stress in varying matrices

	Slurry w/c 0.6	Slurry w/c 0.4	Mortar w/c 0.6
τ_{max} (MPa)	2.96	3.4	5.5

diameter, which is reassuring. On the other hand, it is a well-known fact that stress intensity varies according to the quality of the matrix (water/cement and sand/cement), which is the case here, and also according to the state of the fiber surface itself, which does not allow an intrinsic judgment on values to be made.

2.2. The case of a semicircular fiber

A more common case in practice is that of nonstraight wire-drawn fibers. An experimental program has been carried out using a specially designed fiber geometry, sufficiently simple to validate our model. It is a fiber in a semicircular form attached to two straight segments (Fig. 11). With such a fiber geometry, when the fiber starts to slide, curvature change only occurs at two small regions, part of the straight portion at the end that enters the semicircle and part of the semicircle that moves towards the pulled end and becomes straight. A large part of the semicircle is simply rotating about its center without any curvature change. Along the straight part of this fiber, only cohesion is acting. Finally, friction acts only in the semicircle part on the fiber in addition with cohesion.

The variables used in this program would be fiber diameter, semicircular curvature radius, and matrix nature:

fiber diameters: 0.6 and 1 mm

curvature radius of half-circles: 3, 4, and 5 mm

straight parts length: 7 mm

matrices: slurry (w/c 0.6); slurry (w/c 0.4); mortar (w/c 0.5, sand 5 mm)

steel plastification stress: 1200 MPa

In all, 12 selected configurations were tested with three samples for each. The model was fit in terms of friction coefficient and maximum cohesion stress. Figs. 12 and 13 illustrate the behaviors observed during pullout for two typical different configurations and the fitting of the model.

First of all, it should be noted that the proposed model allows to fit the experimental pullout behaviors quite well. It appears that the maximum cohesion stress that leads to the

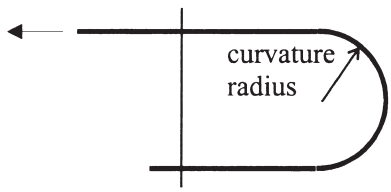

Fig. 11. Geometry of the semicircular fiber.

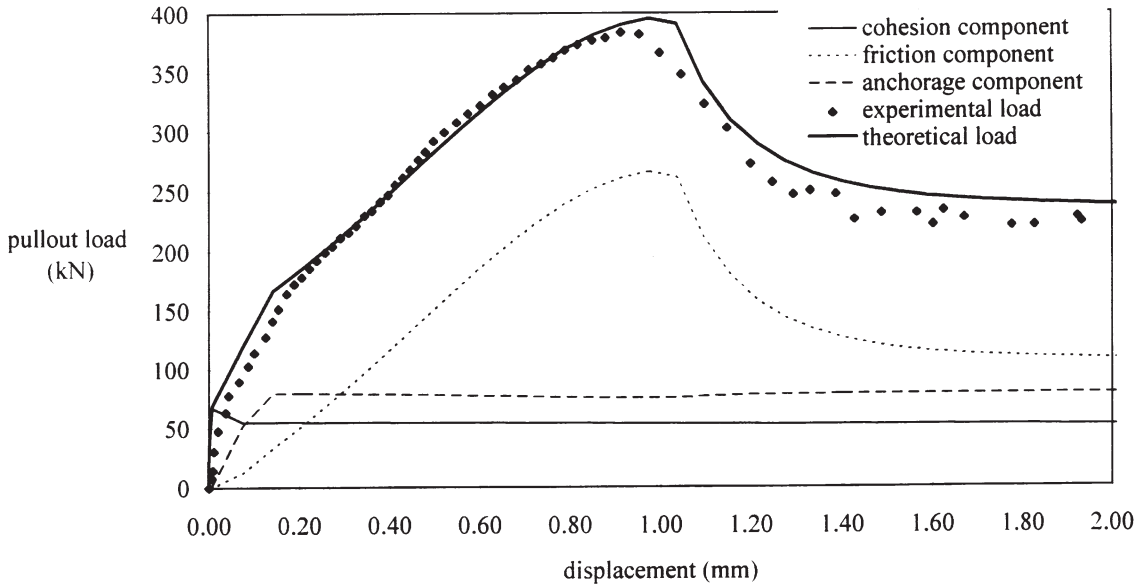

Fig. 12. Pullout load-displacement curves in case of a semicircular fiber (diameter 1 mm, curvature radius 4 mm, mortar).

best visual fit of the model is always lower in case of semicircular fiber than in case of straight fiber. This may come from shrinkage of the matrix, which is more damageable since the fiber geometry is in a plane.

Based on the experimental results, we have sought parameters for modeling the friction coefficient. Independent of matrix variables, fiber diameter, and curvature radius, we obtained values that were noticeably constant in the 12 configurations for the f_{max} and f_{lim} coefficients. The f_{max} value was equal to 0.60 with a standard deviation of 0.07, and the f_{lim} value was equal to 72% with a standard deviation of 7% (fraction of f_{max} after polishing).

As for the modeling slope (α) that characterizes the interface polishing speed, an average value of about 0.4 was nevertheless fitted with a higher typical gap of around 0.1. We can therefore consider that these three coefficients are intrinsic parameters of fiber behavior.

Fitting the relative displacement δo is more complex. Indeed, Fig. 14 illustrates the relative displacement values according to the maximum intensity of pullout load. It clearly

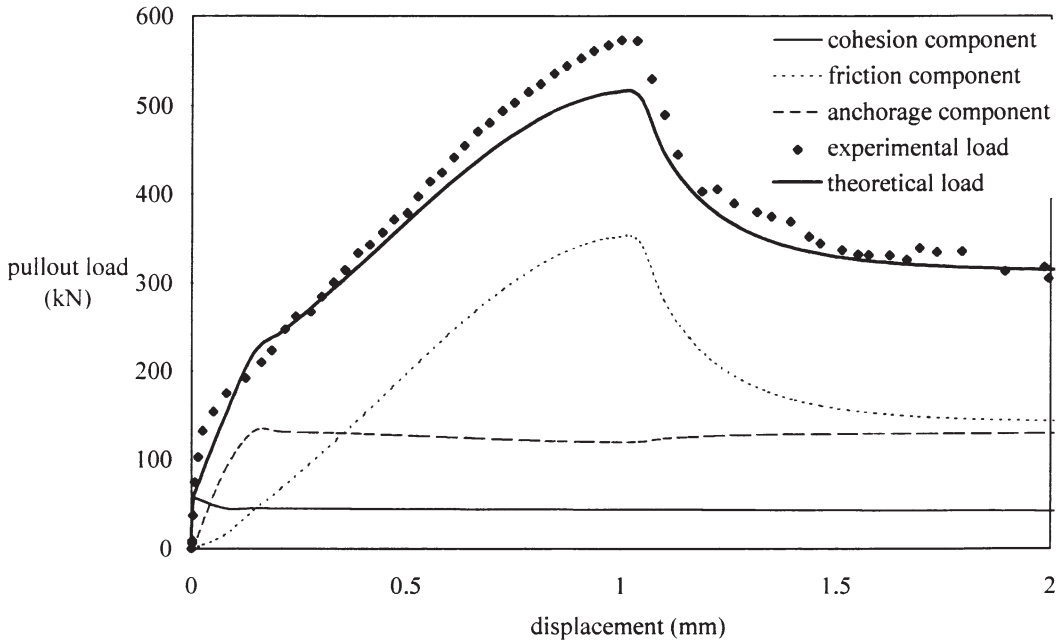

Fig. 13. Pullout load-displacement curves in case of a semicircular fiber (diameter 1 mm, curvature radius 3 mm, slurry w/c 0.6).

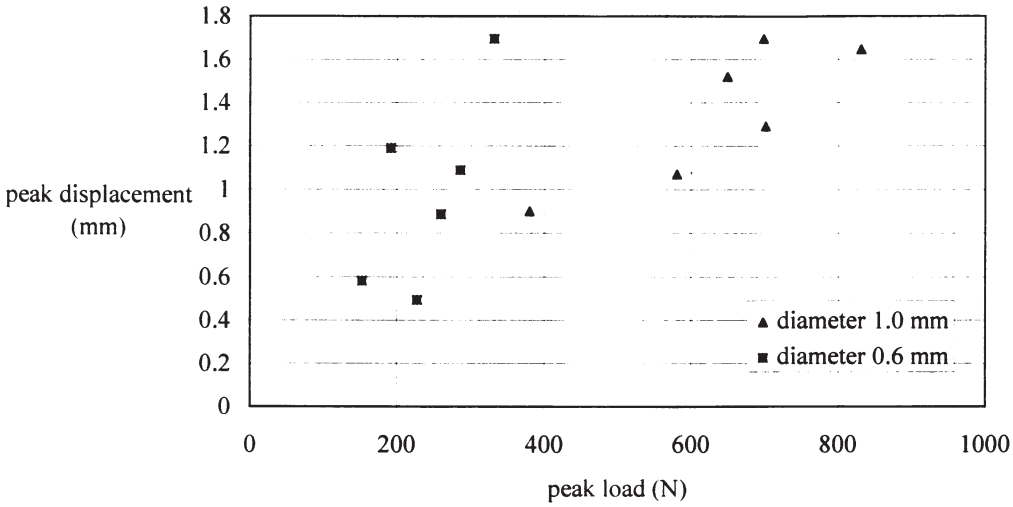

Fig. 14. Friction relative displacement vs. peak pullout load.

appears that there cannot be a single value for the δ*o* displacement. Moreover, an effect can clearly be seen in Fig. 14 as the intensity of pullout load increases, δ*o* displacement increases and two scatterings of points are quite distinct according to fiber diameter. This phenomenon can be explained by considering a slight adaptation of the matrix to fiber movement. Thus, the trend observed on the δ*o* displacement is consistent, taking into account that the higher the pullout load and the shorter the fiber radius, the greater the normal stress applied by the fiber on the matrix. This result was able to be confirmed experimentally by measuring the delay between the displacements of the output and input extremities of the fiber, which is around one-tenth of a millimeter.

Finally, by dividing the maximum pullout load by the fiber diameter, which defines reduced load, we obtained Fig. 15. In spite of the relative dispersion of the points, a good correlation is obtained between peak displacement and this reduced load, independent of fiber diameter. This may allow the model to be predictive whatever the maximum pullout load.

The results obtained from all the fitted coefficients are illustrated in Figs. 12 and 13. Each curve represents one of the components of the model (cohesion, friction, anchorage). First of all, a good reproduction of experimental results was obtained using our model. In addition, we note that the predominant terms of the model in nonstraight wire-drawn fiber behavior are first friction and then anchorage. Cohesion plays only a minor role for these fiber geometries.

3. Applying the model on improved fiber geometries

3.1. The case of a hooked-ends fiber

The geometry of a hooked-ends fiber allows development of an anchorage at the anchored ends of the fiber. When the

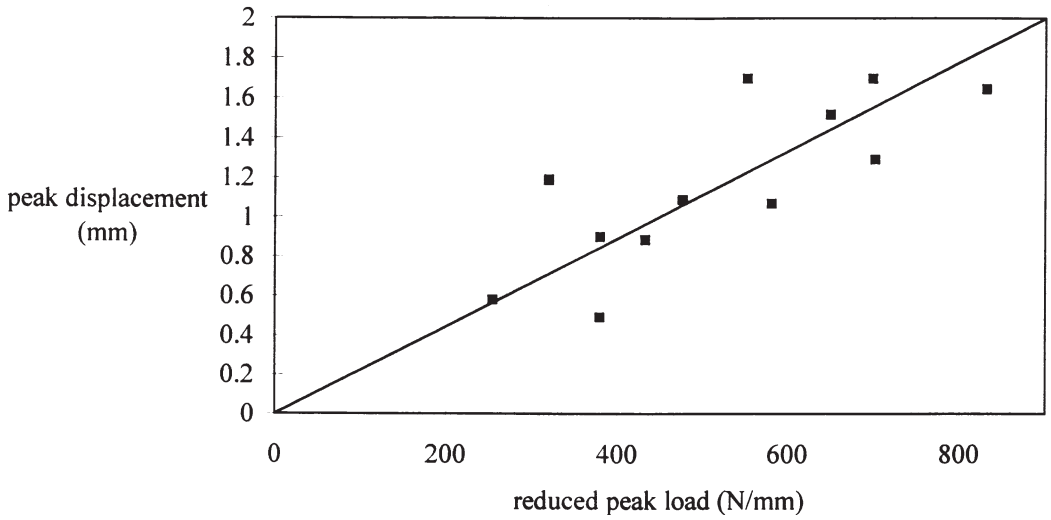

Fig. 15. Friction relative displacement vs. reduced peak load.

pullout stress increases on such a fiber, first there is a debonding and then the fiber slips, which tends to straighten out one of the hooks [1,2,7]. Such a fiber has been modeled through a succession of straight segments and areas of constant curvature (Fig. 16). The modeled fiber has a diameter of 0.8 mm and a plastification stress of 1100 MPa.

The experimental matrix a w/c 0.4 mortar and a cohesion of 5 MPa was used. The friction parameters corresponded to the preceding obtained results, meaning $f_{max} = 0.6$, $f_{lim} = 0.72$, and for the maximum friction displacement, a value of 0.88 mm was adopted in accordance with Fig. 15, with a maximum experimental load of about 320 N.

Fig. 17 illustrates the experimental results and the theoretical simulation. An excellent concordance has been obtained between the two curves from a qualitative point of view. The theoretical curve presents discontinuities in load as the fiber is pulled out, which arises from the discontinuity of curvature in the fiber modeling. These discontinuities are also present but are less pronounced on the experimental curve because of a geometry that is certainly more continuous or that adapts itself progressively during pullout.

A slight overestimation was observed in the theoretical prediction in relation to the experimental results in the maximum load area. This could come again from modeling of the geometry or could simply be an experimental phenomenon, such as a local adaptation of the matrix to the fiber.

3.2. The case of a corrugated fiber

The corrugated fiber represents a very interesting theoretical case. Indeed, the same deformation pattern was reproduced several times along the fiber. The geometry of such a fiber was modeled through a succession of straight segments and circular arcs. Positioning this fiber in relation to the crack corresponds to the experimental configuration illustrated in Fig. 18. During such a pullout experiment, local crushing in the matrix takes place in the crack area that, on one hand, progressively reduces the length of the anchored portion of the fiber and, on the other hand, slightly increases the value of the displacement through fiber local unfolding [23].

To take this effect into account, we modeled the progressive appearance of a matrix cone crushed in the crack opening as the pullout stress increased. Thus, observation of samples showed that the crushed matrix cone has a depth of several millimeters [23]. Good correlation between these observations would be to assume that the length freed by the crushing of the matrix is approximately the pullout load divided by a constant of about 250. For a load of 500 N ap-

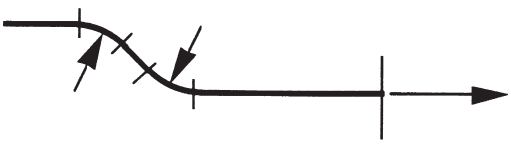

Fig. 16. Modeling a hooked-ends fiber.

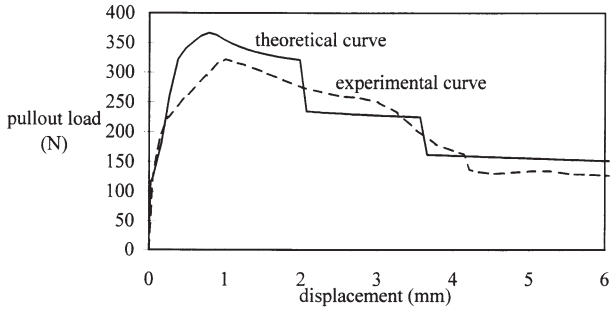

Fig. 17. Pullout curves in the case of a hooked-ends fiber.

plied on such a fiber, the cone therefore reduces the anchored area of the fiber by about 2 mm.

Fig. 19 presents the experimental and theoretical results obtained from the model. We have maintained the preceding intrinsic values for the friction coefficients, meaning $f_{max} = 0.6$, $f_{lim} = 0.72$. A displacement of 1.3 mm, which corresponds to maximum friction, was used, taking into account the intensity of the load obtained experimentally and in accordance to Fig. 15 (the fiber had a diameter of 0.85 mm). The matrix in which the fiber was anchored is microconcrete with a w/c of 0.7 and therefore a cohesion of 5 MPa was adopted. Please note that the experimental program from which this result is taken has already been able to show that the w/c relationship was insignificant in pullout behavior of this fiber geometry [23]. Finally, the steel plastification stress is 1050 MPa.

Overall, the model does an excellent job of describing the behavior of the fiber during pullout. We obtained discontinuities in load on the theoretical curve that correspond to discontinuities in the curvature along the fiber's geometry. These discontinuities are also present on the experimental curve in a less pronounced manner, certainly because of the transition in terms of a more continuous curvature in the actual geometry. We also noted that the theoretical load cancels itself out more rapidly at the end of pullout than the experimental load does. This behavior can be explained by considering on one hand the approach adopted for local matrix crushing. This certainly develops areas of intense curvatures. On the other hand, steel presents various mechanical characteristics after folding and unfolding following proba-

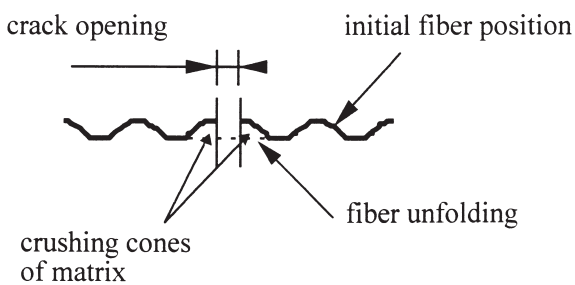

Fig. 18. Modeling a corrugated fiber.

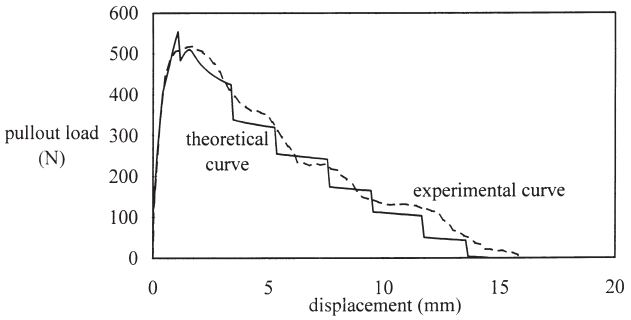

Fig. 19. Pullout curves in case of a corrugated fiber.

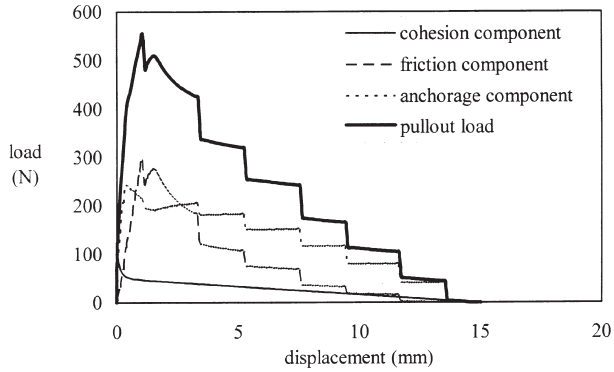

Fig. 20. Various components of the model in case of a corrugated fiber.

ble hardening. These two effects are not taken into account in the theoretical approach that restricts the validity of the model to a few millimeters displacement.

It is interesting to note that towards the peak loading of Fig. 19, we have a discontinuity in load on the theoretical curve. This arises from the effect of the crushed matrix cone that, considering the experimental configuration, frees the fiber on the initial curve area.

Finally, it is interesting to analyze the development of various components of the model, illustrated in Fig. 20. It clearly appears that the cohesion component remains very weak. The high pullout load, which corresponds to the limited crack opening, results from a combination of friction and mechanical anchoring components. Finally, for large crack openings at the end of fiber pullout, it is essentially mechanical anchoring that prevails.

4. Synthesis

It is now interesting to explore how the model can be used to predict the pullout behavior of fiber in a general case. First of all, in case of improved fiber geometry, the cohesion component remains weak and friction and mechanical components are dominant. So in the case of using classical cementitious matrices, an average value of 4 MPa for the maximum cohesion stress will give a good approximation of the cohesion component.

Concerning the friction, we can consider that these coefficients are intrinsic parameters of fiber behavior in classical cementitious matrices. Average values are $f_{max} = 0.60$, $f_{lim} = 72\%$ (fraction of f_{max} after polishing) and slope (α), which characterizes the interface polishing speed at about 0.4. For the peak friction displacement, as this parameter depends on the peak pullout load, fixed value cannot be proposed. Nevertheless, the correlation between peak friction displacement and maximum pullout load can be used at first, as seen in Eq. (24):

$$\delta_0 = \frac{P}{450 \cdot d} \tag{24}$$

where P is the load (N), d is the fiber diameter (mm), and δ_0 is the peak friction displacement

So, while the pullout load increases when the fiber starts to slide, the peak friction displacement is reestimated. When the peak pullout load is reached (the pullout load starts to decrease), the peak friction displacement is memorized and kept constant until the end of the fiber pullout. This method does not affect the general response of the model and only a very small overestimation of the pullout load is obtained before the peak pullout load. In addition, such a way allows the model to be predictive whatever the maximum pullout load. Finally, steel plastification stress is usually between 1050 and 1200 MPa for actual commercialized wire-drawn fibers.

Therefore, the model can be used for predicting pullout behavior of fiber having various geometry. Geometry can be simply modeled by a succession of straight elements and constant curvature elements. A more sophisticated approach is always possible by defining the geometry with a succession of mathematical functions and by calculating numerically the curvature along the fiber.

5. Conclusion

The behavior of metal fibers in cement-based matrices has already been the subject of a very large number of experimental programs. Whether they are experiments at the scale of fiber-reinforced matrices, with their distribution being random or controlled, or even experiments at the scale of individual fibers, these studies have often enabled the behavior of the fibers themselves to be analyzed from an essentially qualitative point of view.

In fact, fiber geometry is the main parameter for reinforcement efficiency that it offers in cracks. We have limited ourselves to the case of wire-drawn steel fibers that, up to now, represent the majority of commercialized fibers. In this case, fiber pullout takes place by a slipping of the fibers in the print of their initial geometry. Therefore, the fiber is straightened, dissipating friction energy and plastification energy, during the slipping process.

Numerous models have been developed in order to characterize this behavior based on the cohesion-slip stress rela-

tionship. It is shown in this paper that each of the phenomena that was observed during the experiments can be modeled in a simple manner and that the overall behavior of a fiber results in an interaction of these phenomena on a local scale.

Several experimental programs have enabled the parameters that are part of the modeling process to be quantified and to show that some of these can be considered as intrinsic properties of the fiber-cement-based matrix association in the most common cases. Finally, various simulations on the geometries of relatively complex fibers that are currently commercialized have enabled our approach to be validated, both quantitatively and qualitatively.

With this new predictive tool, it will now be possible to generate fiber behavior with different geometries. Further developments are needed on the base of local stress analysis to take into account the local crushing effect in crack plane in order to extend the model for variable fiber positionings in relation to crack. Therefore, the proposed model allows more objectivity while describing the fiber behavior and it may be used to optimize fiber geometry.

References

[1] N. Banthia, J.-F. Trottier, ACI Mater J 91 (5) (1994) 435–446.
[2] G. Chanvillard, Etudes et Recherches des Laboratoires des Ponts et Chaussées, Série Ouvrages d'Art, LCPC, Paris, 12, 1993.
[3] V.S. Gopalaratnam, J. Cheng, Proc MRS 114 (1987) 225–231.
[4] R.J. Gray, J Mater Sci 19 (3) (1984) 861–870.
[5] R.J. Gray, J Mater Sci 19 (5) (1984) 1680–1691.
[6] S. Mindess, S Symp Proc MRS 114 (1987) 3–10.
[7] G.G. Namur, A.E. Naaman, ACI Mater J 86 (1) (1989) 45–57.
[8] A.E. Naaman, G.G. Namur, J.M. Alwan, H.S. Najm, J of Struc Engi 117 (9) (1991) 2769–2790.
[9] A.E. Naaman, G.G. Namur, J.M. Alwan, H.S. Najm, J of Struc Engi 117 (9) (1991) 2791–2800.
[10] G. Chanvillard, Int. Symp. BMC4, Warsaw, Pologne, 1994, pp. 311–319.
[11] G. Chanvillard, Int. Symp. on Fibre Reinforced Cement and Concrete, RILEM, Sheffield, UK, 1992, pp. 380–389.
[12] G. Chanvillard, P.-C. Aïtcin, Symp. Proc. MRS, Vol. 211, 1991, 197–202.
[13] G. Chanvillard, P.-C. Aïtcin, Int. Workshop on High Performance Fiber Reinforced Cement Composites, Ed. E & FN SPON, Mainz, 1992, pp. 467–478.
[14] A.M. Brandt, J of Mater Sci 20 (11) (1985) 3831–3841.
[15] J. Morton, G.W. Groves, J of Mat Sci 9 (9) (1974) 1436–1445.
[16] A.E. Naaman, S.P. Shah, J of Struc Div, ASCE 102 (8) (1976) 1537–1549.
[17] C. Ouyang, A. Pacios, S.P. Shah, J of Engi Mech 120 (12) (1994) 2641–2659.
[18] S.P. Shah, C. Ouyang, J Am Ceram Soc 74 (11) (1991) 2727–2738 and 2947–2953.
[19] P. Bartos, Int J of Cem Comp and Lightweight Con 3 (3) (1981) 1–18.
[20] P. Lawrence, J of Mat Sci 7 (1) (1972) 1–7.
[21] Y. Wang, V.C. Li, S. Backer, Int J of Cem Comp and Lightweight Con 10 (3) (1988) 143–149.
[22] Y. Shao, Z. Li, S.P. Shah, J of Advn Cem Bas Mat 1(1993) 55–66.
[23] G. Chanvillard, P.-C. Aitcin, J of Advn Cem Bas Mat 4 (1) (1996) 28–41.